

Scatter correction improvement based on the Convolution Subtraction Technique in SPECT imaging

Mohsen Zand¹

¹(Department of Computer, Islamic Azad University, Doroud, Iran)

ABSTRACT

SPECT is a tomography technique that can greatly show information about the metabolic activity in the body and improve the clinical diagnosis.

In this paper, a convolution subtraction technique is proposed for scatter compensation in SPECT imaging.

In simulation with Gate, 128 projections were simulated evenly spaced over 360° by a circular orbit, each with 128 bins. Simulation results show that this method is effective in SPECT imaging.

Keywords – Convolution, Scatter, Simulation, SPECT

I. INTRODUCTION

Since the early days of the last century, ionizing radiation in particular gamma-rays, thanks to their penetrating property, are used to image the interior of objects. This is done with an external source of radiation, which illuminates an object and projects the shadows of its internal structure on a detecting surface. Later on, it was shown that a true three-dimensional image can be reconstructed if there is a sufficient number of such two dimensional projections generated by the displacement of the source/detector assembly on a specific space curve. In essence, this reconstruction procedure relies on the inversion of the so-called x-ray transform, which is known since many decades [1], [2].

It should be noted that one can also turn passive objects into radiating ones. For example, in nuclear medicine, this is achieved by injecting a radiotracer such as ^{99m}Tc to produce a nonuniform distribution of the tracer within the patient's body. An image (or projection) can be produced by a parallel-hole collimated gamma camera, set to register 140 keV photons emitted by ^{99m}Tc. If the gamma camera is made to rotate around the patient's body, so as to generate a series of images from distinct view angles, then the tracer distribution hidden inside of the body can be reconstructed. This imaging modality is known as single-photon emission computed tomography (SPECT) [3].

In SPECT 2D projections are acquired with a gamma camera at different angles around the patient. The projections are used for reconstruction of a 3D image volume, which ideally should correspond to the activity distribution in the patient. A continuous acquisition of data is possible but requires complicated data management, and in most cases a "step and shoot" technique is used instead, with no data collected during the detector movements. The 2D projections are acquired in a circular or elliptical orbit around the patient, and the number of projections usually varies between 64 and 128, equally distributed in space. A complete acquisition measures projections over a 360°

rotation but a restricted acquisition of 180° is sometimes used. A multiple head system is advantageous for SPECT since it is a relatively time-consuming procedure.

In SPECT, because of photoelectric absorption and Compton scattering, the emitted gamma photons are attenuated inside the body before arriving at the detector. Thus the photon is not necessarily completely stopped but may be scattered. Scattered photons are diverted from their original path with some loss in energy.

In practice some of the scattered photons are still detected within the photo-peak energy window and are physically deflected, so as to be mis-positioned. Although scatter and attenuation are closely linked, when correction is applied the two effects are considered separately; attenuation involves loss of counts whereas scatter involves the detection of additional misplaced counts (see Fig. 1).

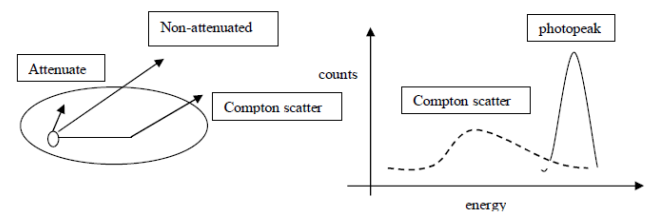


Figure 1: Compton scatter photons lose energy as a result of the deflection but, due to the limited energy resolution of the gamma camera the scattered photons may still be detected in the photo-peak.

The extent of attenuation can be quantified mathematically by the transmitted fraction (TF (t' , s' , θ)), which is the fraction of the photons from location (t' , s') that will be transmitted through a potentially non-uniform attenuator at angle θ . The transmitted fraction is given by (1):

$$1: TF(t', s', \theta) = \exp\left(-\int \mu(t', s') ds\right)$$

where $\mu(t', s')$ is the distribution of linear attenuation coefficients as a function of location.

To account for the presence of scatter, this Equation can be modified by multiplying the exponential term by a buildup factor (B) [4]. The buildup factor is the ratio of the total number of counts detected within the energy window (primary plus scatter) to the number of primary counts detected within the window. In the "good geometry" case there is no scatter detected, so the buildup factor is 1.0.

Thus one can use energy windowing to reduce the amount of scattered photons imaged, but not eliminate scatter, due to the presence of classically scattered photons and the finite energy resolution of current imaging systems. In fact, the ratio of scattered to primary photons in the photo-peak energy window (scatter fraction) is typically 0.34 for Tc-99m [5] and 0.95 for Tl-201 [6]. When scatter is neither removed from the emission profiles prior to reconstruction nor incorporated into the reconstruction process, it can lead to over-correction for attenuation because the detected scattered photons violate the “good geometry” assumption of (1).

Several methods for the effects of scattered events have been proposed. The difference between methods is the way of estimating the scatter contribution. For example some methods involve events collection in one or more energy windows lower than the photo-peak one, and these data can be subtracted from the true data, before or after reconstruction. Other methods try to estimate the shape of the scatter component within the photo-peak window as a convolution of the photo-peak projection with the scatter distribution function.

The proposed method in this paper is based on convolution subtraction but uses wavelet to create matrix of scatter fractions instead of a global scatter fraction. In these techniques scatter correction in the projection relies on filter functions, evaluated by wavelet.

The aim of this work is try to estimate the shape of scatter within photo-peak window as a convolution of the lower energy projection (86-100keV) with the wavelet transform. The scatter projection was calculated from measurements of a 99mTc line source in a water cylindrical phantom within both photo-peak and lower energy windows. Then the term of calculated scatter was subtracted from photo-peak window (scatter plus primary). Gate software package was used for simulation and MATLAB software was used to design a 2D wavelet filter for estimating scatter in photo-peak. Finally their results were used to correct scatter for a more realistic phantom such as NCAT.

II. METHODS AND MATERIALS

Scatter corrections based on convolution or deconvolution were introduced by Axelsson et al [7] as a 1D method which was further developed to 2D by Msaki et al [8]. These methods take the spatial distribution of the scattered photons into account instead of the energy spectra. The methods operate on geometrically mean valued images to decrease the depth dependence. A scatter kernel describes the spatial distribution of the scattered photons, which in most cases, but not always [9], is assumed to have mono-exponential form. The exponential describing the fall-off of the scatter kernel is called “slope” in this work. Methods based on deconvolution use a one-step operation to calculate the scatter corrected image [8, 10] whereas methods based on convolution can be seen as two-step operations [6]. For the 2D two-step operation, convolution scatter subtraction, the geometric mean valued image of primary registrations $g(x,y)$ can ideally be calculated as (2) [11]:

$$2: g(x, y) = g_{\text{obs}}(x, y) - k_p(g(x, y) \otimes s)$$

where g_{obs} is the observed, non-corrected geometrically mean valued projection image, k_p is the scatter-to-primary ratio and s is the stationary scatter kernel. In this equation the image of primary registrations appear on both sides, and an approximation is therefore used where the original image is convolved with the scatter kernel (3):

$$3: g(x, y) = g_{\text{obs}}(x, y) - k_T(g_{\text{obs}}(x, y) \otimes s)$$

k_T in this equation is the scatter-to-total ratio. The method is based on the approximation that both the scatter-to-total ratio and the slope of the scatter kernel are constant. For a uniform object such as a cylindrical water phantom with uniform activity, this approximation is not too serious, but the severity of the approximation will increase for more inhomogeneous source distributions and density variations [12]. Instead of using a global scatter fraction as for convolution scatter subtraction, a scatter fraction is calculated for each pixel in the image to be corrected. In this way one of the stationary factors in convolution scatter subtraction is removed. The scatter fractions can be calculated from transmission measurements but they can also be calculated from ray sums through an attenuation map obtained by some other method, for example from CT images. This scatter correction technique can therefore easily be implemented if a non-uniform attenuation correction is utilized.

TDCS has been shown to give quantitative results with an accuracy better than 95% in the heart and lung region in a thorax phantom [13]. Quantitative results that are more accurate than results obtained using the TEW scatter correction technique and with a higher signal to noise ratio have also been demonstrated for simulations and measurements of a chest phantom. The primary source of weakness lies in the fact that it is a 2D method with a scatter kernel that is independent on object thickness and source distribution. The composition and shape of the object can however be taken into account to some degree because of the spatially varying scatter-to-total ratio.

We have investigated the impact of scatter on “cold” and “hot” tumor detection for Tc-99m -labeled antibody fragments used for hepatic imaging.

The Gate program was used to create 128 SPECT projections of the abdominal region as defined by the Zubal phantom.

The primary and scattered photons were stored in separate data files. Similarly, high-count projections of a 2.5-cm diameter spherical “tumor” in each of 3 locations within the liver were also created via Gate. These projections were scaled and added to (“hot” tumors) or subtracted from (“cold” tumors) the background distribution.

Projections were made with solely the primary photons present. These were used to assess the impact of perfect scatter rejection as might be approximated by imaging with a detector with extremely good energy resolution.

Projections were also made with both the primary and scattered photons present (standard imaging of Tc-99m), and with 2.5 times the scattered Tc-99m photons present.

To get a set of complete data needed for three-dimensional reconstruction, it is necessary to move the detector in space around the object, so as to get all the lines traversing the object in all directions (spaced over 360° by a circular orbit). Hence for a given single linear projection, only voxels lying on a straight line are concerned. Because of photon attenuation and the presence of a physical collimator, few from these primary photons (actually one out of 10⁴) would actually reach the detector [14].

To provide more convincing arguments regarding the viability of this idea, we use Gate software with the following working conditions:

- the used gamma detector is a conventional SPECT camera. It has discretized dimensions N length units × N length units. We have chosen N = 16 to keep the calculations required at a reasonable level.
- the scattering medium is represented by a cube of dimensions N × N × N,
- the electron density in biological medium is $n_e = 3.5 \times 10^{23}$ electrons/cm³,
- the radionuclide employed is Tc-99 with an activity concentration corresponding to 4.84×10^{10} counts per minutes per cm³,
- the acquisition time per projection is set to 0.1 sec,
- the 3D original object (cylinder of height 6 arbitrary units) is placed at the center of the scattering medium (cube),
- the distance from the camera to the upper face of the scattering medium cube is $l = 200$ arbitrary units.

A 256 × 256 pixels detector is placed on the xy plane. The pixel size is 0.4 × 0.4 mm². The scattering medium is a rectangular box of dimensions 30 cm by 30 cm by 15 cm, which is at a distance of 1 cm above the planar detector. The electronic density inside the scattering medium is $n_e = 3.341023$ electrons/cm³ since most biological tissues have an electronic structure close to that of water. The radionuclide used in this simulation is ^{99m}Tc, which emits photons at an energy of 140.1 keV. The scattering medium is discretized with 13 voxels in x and y axis directions and with 9 voxels in z axis direction. The detector is reduced to 13×13 pixels. We construct the weight matrix of the medium by calculating from our previous models, for each point of the mesh, the PSF of the detector at the different scattering angles. The reconstruction is carried out using the conjugated gradient method with positivity constraint.

The wavelet transform used in the present study is realized through an iterative decomposition algorithm known as the dyadic discrete wavelet transform (dyadic DWT).

Photoelectric absorption is most likely to occur for low photon energies ($h\nu$) and high atomic numbers (Z) of the absorbers, according to the following relation (4):

$$4: \sigma = Z^n / (h\nu)^{7/2}$$

where σ is the atomic cross section for the interaction, which is a measure of its probability. n is between 4 and 5, depending on both $h\nu$ and Z. The photoelectric absorption involves complete absorption of the gamma photon and ejection of a bound electron.

The non-corrected geometrically mean valued projection image is re-normalized by σ according to the following relation (5):

$$5: \beta_\sigma(h, t) = \beta(h, t) \sigma(t)$$

respect to the (x, y) coordinate system then h and t can be written in terms of x and y (6,7), and the rotation angle θ as [15]:

$$6: t = x \cos \theta + y \sin \theta$$

$$7: h = -x \sin \theta + y \cos \theta$$

where h denotes the height and t denotes the time variable.

Our studies show that a simple estimate of a pixel-wise scatter threshold is given by (8):

$$8: eC = 1 + 3\sqrt{2}$$

Based on eC a simple indicator function can be introduced (9):

$$9: I(h, t) = \int \chi \{ \beta_\sigma(\xi, t) > eC \} (\xi, t) d\xi$$

where χ is the characteristic function with $\chi(\xi, t) = 1$ for $\beta_\sigma(\xi, t) > eC$ and $\chi(\xi, t) = 0$ elsewhere. Therefore, at locations (h, t) where $I(h, t) = 0$ we may assume that no scatter are present.

Hence, we may define corrected geometrically mean valued projection image data f (scatter- free) by (10):

$$10: f(h, t) = \beta(h, t) \chi \{ I(h, t) = 0 \} (h, t)$$

with $\chi(h, t) = 1$ for $I(h, t) = 0$ and zero elsewhere.

For temporal averaging, every k profiles are summed (thus reducing the number of profiles to Nt/k). Spatial smoothing is accomplished with a sliding-average length of l height bins (for ceilometer data with a bin width of 15 m, $l = 20$ is typical). The averaged data, $F(h, t)$, are then used for the wavelet analysis.

The final step of the this procedure is the gradient analysis of $F(h, t)$ of each individual spatial measurement, i.e. for each individual t. We define the wavelet transform as (11):

$$11: W_\psi F(h, a; t) = 1/\sqrt{c\psi} \int F(\gamma, t) 1/\sqrt{a} \psi((\gamma-h)/a) d\gamma$$

Where the normalization constant $c\psi$, given by (12):

$$12: 0 < c\psi = 2\pi \int |\psi(\omega)|^2 / |\omega| d\omega < \infty$$

reflects the constraint on the analyzing wavelets to produce an invertible and isometric transform. The isometric property is relevant since it ensures norm equality between the signal F and its wavelet transform (allowing a physical interpretation of the wavelet-transformed signal). ψ^\wedge denotes the Fourier transform of the analyzing wavelet.

which allows one to analyze also the behavior of derivatives of F of higher order, and this can give a hint at where the gradient growth (or decay) becomes maximum or minimum (C is a constant).

Our algorithm uses the Daubechies wavelet family (1st, 2nd, 3rd order) [15], thus yielding more structural information on the signals to be analyzed. In order to detect scatter, we evaluate the wavelet spectrum at all scales simultaneously.

This can be easily done by temporal spectrograms (13),

$$13: S(h, t) = \int |W\psi F(a, h; t)|^p da$$

With $p > 0$, which can alternatively be replaced by (14):

$$14: S(h, t) = (\int |W\psi F(a, h; t)|^p \text{sing}[W\psi F(a, h; t)] da$$

This equation additionally takes into account the sign of the gradient information (which is, for our purpose, rather important).

In general, the evaluation of S(h, t) will not yield a single, unique scatter function but a set of scatter candidates.

III. RESULTS

Two simulations of the Zubal phantom with an activity distribution were then performed one allowing scatter, and one without scatter. The images without scatter can be seen as the ideal images. The images including scatter were scatter corrected using parameters for the geometries, and for each geometry a range of different scatter kernel slopes were applied (Fig.2). The images compared with the reconstructed ideal image volume by means of the normalized mean square error (NMSE) [16]. NMSE quantifies the difference between the corrected images and the ideal images.

This simulated study showed that the method improves the image quality and quantitative accuracy up to 1.5 dB in comparison to scatter reduction in the convolution-based method (Fig.3).

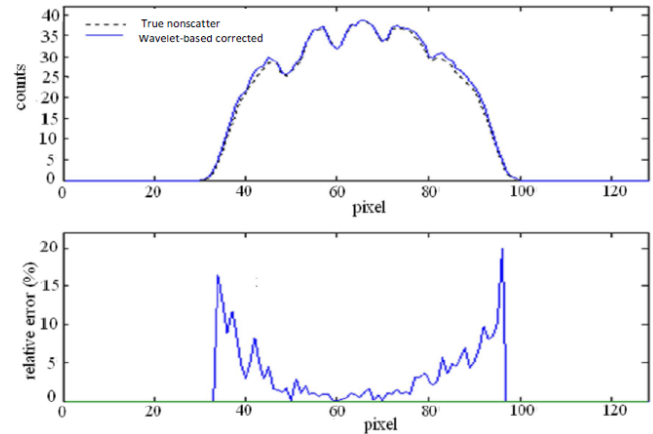


Figure2: Profile image including scatter that were scatter corrected and relative error.

For both simulations, primary images gave a statistically significant increase in detection accuracy in comparison to the images with an artificially elevated amount of scatter. Here the difference in areas was larger (0.88 versus 0.81 for cold tumors, and 0.84 versus 0.74 for hot tumors). In no case did scatter compensation result in a statistically significant increase in detection accuracy over any compensation. However, with the artificially elevated amount of scatter the areas did increase with scatter compensation (0.81 with no compensation versus 0.83 with scatter compensation for the cold tumors, and 0.74 with no compensation versus 0.78 with scatter compensation for the hot tumors).

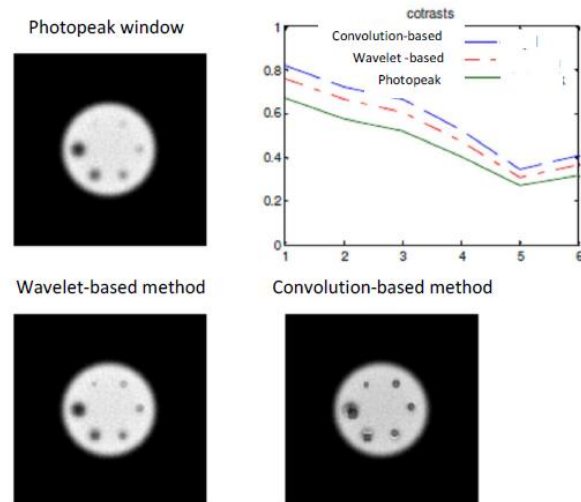


Figure3: comparison between scatter reduction in the convolution-based method and wavelet-based method

IV. CONCLUSION

The reconstruction results from computer simulations show that the wavelet-based SPECT reconstruction algorithm is accurate.

In summary, the results obtained with our algorithm are promising, but the quality of the retrieval has to be assessed in future studies. Questions that have to be addressed in this context evolve around the definition of scatter in general, and the threshold and parameter values used in the retrieval algorithm.

To evaluate accurately the spatial resolution, it is necessary to use real data and to compare it with conventional methods which do not make use of scattered radiation. At the present time, it is too early to use our preliminary simulation results for this purpose. This work is ongoing using realistic experimental conditions.

ACKNOWLEDGEMENTS

My friend and coworker Mohammad Seifabadi for support, encouragement and for sharing your inspiring ideas with me.

REFERENCES

- [1] H Tuy, An inversion formula for cone-beam reconstruction, *SIAM J. Appl. Math.*, vol. 43, pp. 546-552, 1983.
- [2] S Zhao, H Yu and G Wang, A unified framework for exact cone-beam reconstruction formulas, *Med. Phys.*, vol. 32, pp. 1712-1721, 2005.
- [3] Wernick M, Aarsvold J. Emission Tomography: *The Fundamentals of PET and SPECT* (San Diego, Academic Press, 2004).
- [4] Attix FH. *Introduction to Radiological Physics and Radiation Dosimetry* (John Wiley & Sons, New York, 1983).
- [5] de Vries DJ, King MA. Window selection for dual photo-peak window scatter correction in Tc-99m imaging. *IEEE Trans Nucl Sci* 41:2771-2778, 1994.
- [6] Hademenous GJ, King MA, Ljungberg M, Zubal G, Harrell CR. A scatter correction method for Tl-201 images: a Monte Carlo investigation. *IEEE Trans Nucl Sci* 30:1179-1186, 1993.
- [7] Axelsson B, Msaki P, Israelsson A. Subtraction of Compton-scattered photons in singlephoton emission computed tomography. *J Nucl Med* 1984 25: 490-494
- [8] Msaki P, Axelsson B, Dahl CM, Larsson SA. A generalized scatter correction method in SPECT using point scatter distribution functions. *J Nucl Med* 1987 28: 1861-1869
- [9] Narita Y, Eberl S, Iida H, Hutton BF, Braun M, Nakamura T, Bautovich G. Monte Carlo and experimental evaluation of accuracy and noise properties of two scatter correction methods for SPECT. *Phys Med Biol* 1996 41: 2481-2496
- [10] Floyd CE, Jaszczak RJ, Greer KL, Coleman RE. Deconvolution of Compton scatter in SPECT. *J Nucl Med* 1985 26: 403-408
- [11] Msaki P, Erlandsson K, Svensson L, Nolstedt L. The convolution scatter subtraction hypothesis and its validity domain in radioisotope imaging. *Phys Med Biol* 1993 38: 1359-1370
- [12] Msaki P. Position-dependent scatter response function: will they make a difference in SPECT conducted with homogeneous cylindrical phantoms, *Phys Med Biol* 1994 39: 2319-2329
- [13] Meikle SR, Hutton BF, Bailey DL, Fulton RR, Schindhelm K. SPECT scatter correction in non-homogeneous media. In: Colchester A C F and Hawkes D J, eds. *Information processing in medical imaging, 12th international conference*. Berlin: Springer-Verlag 1991 34-44
- [14] Brooks, I.M. 2003: Finding boundary layer top: application of a wavelet covariance transform to lidar backscatter profiles. *J. Atmos. Ocean. Technol.*, 20, pp. 1092-1105.
- [15] Daubechies, I. *Ten Lectures on Wavelets* (SIAM, Philadelphia, U.S.A., 1992).
- [16] King MA, Schwinger RB, Penney BC. Variation of the count-dependent Metz-filter with imaging system modulation transfer function. *J Med Phys* 1986 13: 139-149.